

Detection of Iron in Nanoclustered Cytochrome C Proteins Using Nitrogen-Vacancy Magnetic Relaxometry

Suvechhya Lamichhane,¹ Rupak Timalisina,² Cody Schultz,³ Ilja Fescenko,⁴ Kapildeb Ambal,⁵ Sy-Hwang Liou,¹ Rebecca Y. Lai,³ and Abdelghani Laraoui^{1,2,*}

¹*Department of Physics and Astronomy and the Nebraska Center for Materials and Nanoscience, University of Nebraska-Lincoln, Lincoln, Nebraska 68588, USA*

²*Department of Mechanical & Materials Engineering, University of Nebraska-Lincoln, Lincoln, NE 68588, USA*

³*Department of Chemistry, University of Nebraska-Lincoln, Lincoln, NE 68588, USA*

⁴*Laser Center, University of Latvia, Riga, LV-1004, Latvia*

⁵*Department of Mathematics, Statistics, and Physics, Wichita State University, Wichita, KS 67260, USA*

ABSTRACT: Nitrogen-vacancy (NV) magnetometry offers an alternative tool to detect iron levels in neurons and cells with a favorable combination of magnetic sensitivity and spatial resolution. Here we employ NV- T_1 relaxometry to detect Fe in cytochrome C (Cyt-C) nanoclusters. Cyt-C is a water-soluble protein that contains a single heme group and plays a vital role in the electron transport chain of mitochondria. Under ambient conditions, the heme group remains in the Fe⁺³ paramagnetic state. We perform NV- T_1 relaxometry on a functionalized diamond chip and vary the concentration of Cyt-C from 6 μ M to 54 μ M, resulting in a decrease of T_1 from 1.2 ms to 150 μ s, respectively. This reduction is attributed to spin-noise originating from the Fe spins present within the Cyt-C. We perform relaxometry imaging of Cyt-C proteins on a nanostructured diamond by varying the density of adsorbed iron from 1.44×10^6 to 1.7×10^7 per μm^2 .

KEYWORDS: *Nitrogen-vacancy, relaxometry, cytochrome C, iron, biosensing*

Cytochromes, including cytochrome C (Cyt-C), are redox-active proteins involved in the electron transport chain (ETC) and redox catalysis. Cyt-C is a 13 kDa water-soluble heme protein typically located in the inter-mitochondrial membrane.^{1,2} The main function of Cyt-C within the mitochondria is to act as an intermediate electron receptor for respiration, namely to move electrons between Complex III and Complex IV.¹ In the ETC, an electron is transferred from Complex III to the heme group of the oxidized Cyt-C (Fe⁺³) which reduces it to Fe⁺². Cyt-C then releases the electron to Complex IV, and the Fe center then returns to the Fe⁺³ oxidized state.³ In mammalian cells, the release of Cyt-C from the mitochondria is linked to cell apoptosis.² During cell necrosis and apoptosis, the Cyt-C is released from the mitochondria, which leads to the non-inflammatory activation of apoptotic protease activating factor 1, eventually cascading to caspase-9 activation and the execution-phase of the cell.⁴ The concentration of Cyt-C in the mitochondria decreases, whereas its concentration increases in the cytosol process. Thus, depending on the specific part of the cell that is being imaged/analyzed, the amount of Cyt-C could be different during apoptosis.^{1,2}

While the inner cellular release of Cyt-C is not linked to inflammation, the release of Cyt-C into the extracellular matrix has been correlated to inflammatory conditions and cellular damage. In one study, rats resuscitated after experiencing ventricular fibrillation showed a peak 10-fold increase of plasma Cyt-C. Furthermore, the survival outcome of the rats was inversely correlated to the plasma Cyt-C concentrations.⁵ Increased Cyt-C levels have also been linked to liver disease,

liver damage, and kidney damage.^{6,7} Therefore, plasma Cyt-C can be a useful diagnostic tool for pathogen-associated or danger-associated molecular patterns.² Current methods for detecting Cyt-C including high-performance liquid chromatography,^{8,9} flow-based paper biosensors,¹⁰ and immunoassays.¹¹

Cyt-C is a heme iron-containing protein Fe (III) (or Fe⁺³) paramagnetic state under ambient conditions.¹ It serves as a mediator of cellular electrical conductivity and is nearly ubiquitous in organisms that generate a proton gradient. Electron transfer reactions in cells utilize metal ions such as iron to mediate flow of electrons from electron donors (*e.g.*, growth substrates, intracellular electron carriers like flavins or nicotinamide adenine dinucleotide, or from an extracellular cathode) to electron acceptors. The terminal electron acceptor may be oxygen in the case of aerobic respiration, other molecules in the case of anaerobic fermentation or respiration, or an extracellular anode.³

Numerous techniques have been utilized to detect iron in Cyt-C, including electron paramagnetic resonance (EPR) spectrometry¹²⁻¹⁴ and X-ray photoelectron spectroscopy (XPS).^{15,16} However, a larger quantity of Cyt-C proteins is required (powder or liquid) to obtain a measurable signal, hindering their applications in detecting Fe at the nanoscale within single cells. The variation of the Cyt-C concentration in the cells depending on the physiology process makes it hard to use bulk techniques such as EPR to detect Fe in Cyt-C at the submicron scale. Among the currently available high-sensitivity and spatial resolution iron detection techniques, magnetic imaging based on the nitrogen-vacancy (NV) center in diamond¹⁷⁻²² emerges as one of the most promising tools for high-resolution nanoscale imaging, particularly for iron-containing proteins such as Cyt-C. The NV center is a spin-1 defect with optically addressable electron spin properties²³⁻²⁵ and millisecond spin relaxation times (T_1 , T_2) at room temperature.²⁶ These capabilities have opened new opportunities in quantum sensing,²⁷ nanoscale magnetometry,²⁸⁻³⁰ and biosensing.³¹ For example, it enabled the initial detection of single proteins,³² perform nanoscale (volume < 1 μm^3) nuclear magnetic resonance (NMR) spectroscopy.³³⁻³⁶ NV magnetometry has been used very recently to measure the magnetic properties of individual (size < 1 μm) malarial hemozoin biocrystals²² and [Fe(Htrz)₂(trz)](BF₄) spin crossover molecules.¹⁷ Another approach of NV magnetometry is to detect magnetic fluctuations or spin noise from metal ions through the decrease of the spin-lattice T_1 relaxation time. NV T_1 relaxometry has been used to detect Gd⁺³ ions,³⁷ Cu⁺² ions,³⁸ and recently to map Fe⁺³ in ferritin proteins.^{20,21} There have been several studies using NV relaxometry in the biomedical field to study free radicals present in single mitochondria,³⁹ Endothelial Cells,⁴⁰ dendritic cells,⁴¹ and virus-infected cells,⁴² providing great insights on understanding the cellular metabolism.

In this paper, we use NV T_1 relaxometry to detect iron in Cyt-C nanoclusters (diameter: 50 – 200 nm, height: 5 – 15 nm) in combination with XPS, EPR, scanning electron microscopy (SEM), and atomic force microscopy (AFM) to measure their respective diameter and height. We vary the concentration of Cyt-C from 6 μM to 54 μM drop-casted on the diamond chip and show a reduction of the NV relaxation time T_1 from ~ 1.2 ms to < 200 μs , explained by the spin-noise generated from the Fe spins present within the Cyt-C proteins. We conduct magnetic imaging of Cyt-C proteins functionalized on top of nanostructured diamond chip, allowing us to detect the density of adsorbed Fe from 1.44×10^6 to 1.7×10^7 per μm^2 .

Cyt-C features a Fe⁺³ center, also known as heme center,¹ which is coordinated to four nitrogen atoms, forming the heme ring as depicted in Figure 1a. Additionally, Fe⁺³ coordinates with methionine and histidine amino acids, resulting in a hexacoordinated configuration.³ Notably, the sulfur atom from the methionine group acts as a strong-field ligand, causing the heme complex

to exhibit a low spin state ($S = \frac{1}{2}$) under ambient conditions.⁴³ In this work, we use horse heart Cyt-C purchased from Sigma Aldrich (molecular weight = 12,384 g/mol). As received, Cyt-C is predominantly in the oxidized state Fe^{+3} and diluted in deionized (DI) water with a density of 200 mg/ml (~ 16.1 mM, pH = 5).

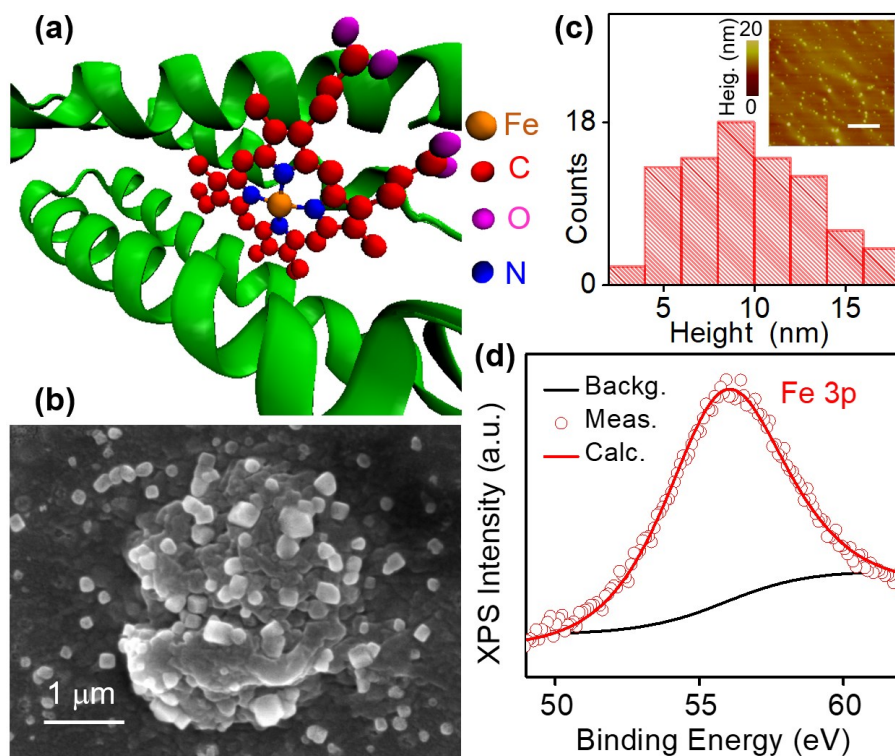


Figure 1. (a) Molecular structure of Cyt-C complex derived from reference [1]. (b) SEM image of 18 μM Cyt-C drop-casted on a carbon tape to prevent charging effect. (c) AFM height distribution of Cyt-C nanoclusters (concentration of 2 μM) drop-casted on top of the diamond substrate. The mean height of Cyt-C nanoclusters is $\sim 9 \pm 6$ nm. Inset of (c): AFM image of the Cyt-C nanoclusters (the scale bar is 5 μm). (d) Measured (open circles) XPS spectra of Fe 3p in Cyt-C with the fitting (red solid line) showing the Fe^{+3} state. The background signal is plotted in the black solid line curve.

To measure the diameter and height of Cyt-C nanoclusters, we further diluted the Cyt-C DI water solution to a concentration of ~ 0.1 mM and drop-casted 5 μL on silicon and diamond substrates, allowing it to evaporate and form a thin film. To prevent from charging effects on SEM measurements, we drop-casted Cyt-C nanoclusters on carbon tape¹⁷ and on gold (Au) coated diamond substrates (see the Supporting Information Section S1). Figure 1b shows the SEM image of nanoclustered Cyt-C proteins on carbon tape with an aggregated diameter that varies from 30 nm to 150 nm (Supporting Information Section S1). The diameter of a single monomer of Cyt-C is reported to be ~ 3.4 nm.⁴⁴ However, due to surface interactions, when Cyt-C is drop-casted on the diamond surfaces, it tends to agglomerate, resulting in larger nanoclusters. Remarkably, even at a lower concentration (≤ 2 μM), this agglomeration phenomenon is still observed on the diamond substrate with an average diameter of Cyt-C nanoclusters observed 100 ± 50 nm (Figure S1). Similar agglomeration effects have been reported across different concentrations of Cyt-C.⁴⁴ Even in its natural state, Cyt-C tends to polymerize rather than remain in a monomeric state, despite its stability, possibly through aggregation.⁴⁵ AFM measurements of 2 μM Cyt-C solution drop-casted on top of diamond substrate show a height of $\sim 9 \pm 6$ nm, Figure 1c.

To further ensure the absence of impurities, XPS measurements were conducted, as detailed in the Supporting Information Section S2. We employed a high-resolution XPS for N, S, C, O, and Fe. Subsequently, we conducted peak fitting using a combined Lorentzian and Gaussian function. Additional details can be found in the Supporting Information Section S2. Figure 1d shows the high-resolution spectra of Fe 3p. The spectra exhibit a distinct peak at a binding energy of 55.6 eV, indicative of the Fe oxidation state being Fe⁺³.⁴⁶ Moreover, we corroborated the presence of Fe-sulfur bonds at binding energy of 167 eV through the examination of the high-resolution sulfur peak, as illustrated in Figure S2d.⁴⁷

The negatively charged NV center in the diamond lattice is a substitutional nitrogen adjacent to a vacancy site (Figure 2b) with a spin triplet in the ground state that features a zero-field splitting $D = 2.87$ GHz between states $m_S = 0$ and $m_S = \pm 1$ (Figure 2c).^{23,25} A green laser illumination (532 nm) yields spin-conserving excitation to the excited triplet state, which in turn leads to far-red photoluminescence (650 – 750 nm). Intersystem crossing to metastable singlet states takes place preferentially for NV centers in the $m_S = \pm 1$ states, ultimately resulting in an almost complete transfer of population to the $m_S = 0$ state.²³ Microwave (MW) excitation allows spin transitions from $m_S = 0$ to $m_S = \pm 1$ sublevels. The applied magnetic field breaks the degeneracy of the $m_S = \pm 1$, leading to a pair of spin transitions ($m_S = 0$ to $m_S = +1$ and $m_S = 0$ to $m_S = -1$) that can be interrogated *via* optically detected magnetic resonance (ODMR) spectroscopy.^{17,22} This method results in a set of resonances (Figure S5b), whose frequencies are sensitive to magnetic fields and temperature. In addition, if the laser excitation is abruptly turned off, the amplitude of the ODMR signal decays exponentially as the NV electron spins relax from their polarized states. The rate of this decay Γ_1 or relaxation time $T_1 = 1/\Gamma_1$ depends on the weak random magnetic fields (or spin noise) created by the diamond sensor itself, as well as external spin noise.^{48,49} Measurements of the rate change Γ_1 is the basis of NV- T_1 relaxometry used here to detect magnetic dipole-dipole interaction between NV spins and the fluctuating Fe⁺³ in cytochrome C (Cyt-C) nanoclusters⁵⁰.

To make the NV sensor, we used 3 mm × 2.5 mm × 0.05 mm electronic grade (100) cut and polished diamond. A thin (a thickness ~ 5 – 8 nm) NV sensing layer (Figure S5a) was created near the diamond surface by using ¹⁵N⁺ implantation (4 keV) followed by high vacuum (down to 10⁻⁶ Torr) high temperature (1100 °C) annealing and cleaning in a boiling tri-acid mixture.^{22,35,51} Additional details regarding the NV sensor fabrication are provided in the Supporting Information Section S5. To attach Cyt-C proteins, we carboxylated the diamond surface with NV layer underneath (see the Supporting Information Section S3). The adsorption of Cyt-C occurs through electrostatic attraction between the anionic groups (–COO⁻) present on the carboxylated surface and the positively charged amino groups (–NH³⁺), or through the formation of hydrogen bonds between –NH³⁺ and any CO⁻.⁵² Various concentrations of Cyt-C in DI water were drop-casted on the NV sensor. We used DI water instead of other buffers to prevent any effects on T_1 from the salts and other compounds present in them.

In Figure 2d, we show the schematic of the widefield ODMR microscope using NV- T_1 relaxometry. We used a 532 nm laser (power = 180 mW) to excite the NVs over an area of ~ 36 μm × 36 μm, and the NV fluorescence (650 – 750 nm) is mapped onto a sCMOS camera.^{17,22} The NV sensor was placed on top of a glass coverslip with patterned gold loops for MW excitation (Figure 2d). A magnetic field B_{app} (3.2 mT) is applied along [111] direction of the (100) diamond enabling the separation of two ODMR peaks each for $m_S = 0$ to $m_S = -1$ and $m_S = 0$ to $m_S = +1$ respectively (Figure S5b). Detailed information regarding the experimental setup is provided in the Supporting Information Section S5.

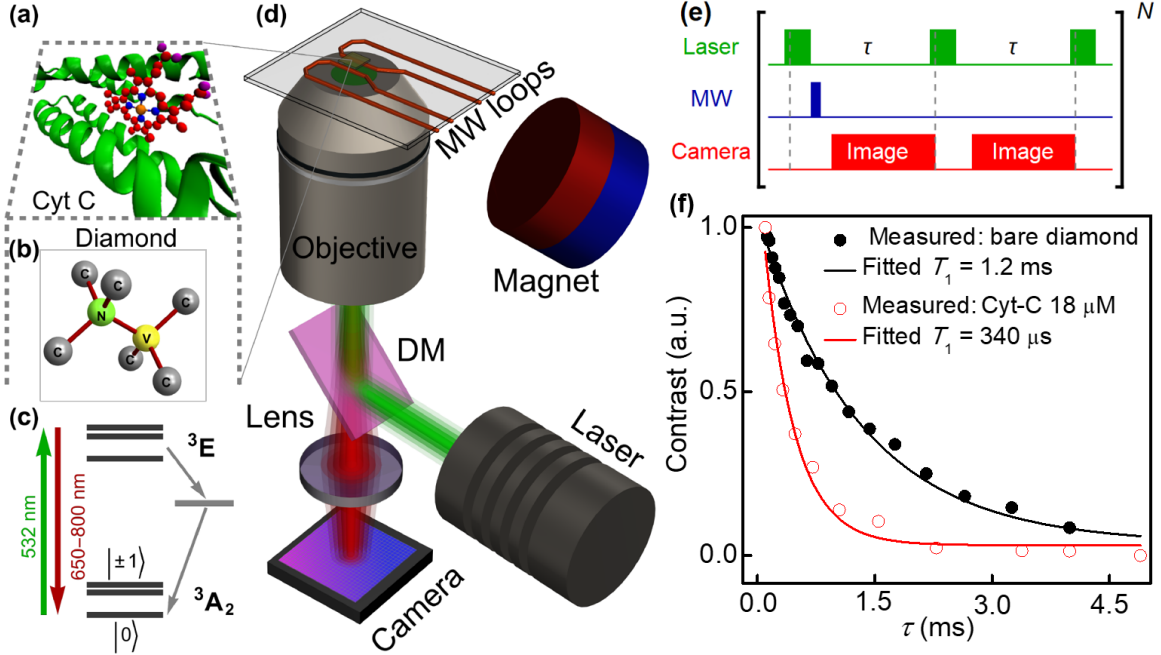


Figure 2. (a) Molecular structure of Cyt-C protein. (b) A schematic of the NV center inside the diamond lattice (nitrogen: green atom, yellow: vacancy). (c) A schematic of the energy levels of the NV center ground (3A_2) and excited (3E) states with intermediate metastable state. A green laser (532 nm) initializes the NV center spins and results in fluorescence in wavelength range of 650 – 800 nm. (d) A schematic of the widefield NV microscope used for T_1 relaxometry measurements and imaging of Cyt-C nanoclusters. DM is the dichroic mirror. (e) A schematic of a pulse sequence for T_1 relaxometry imaging. (f) T_1 curve measured on a bare diamond (filled circles) and after drop-casting 18 μ M Cyt-C solution on diamond (open circles). The black and red solid lines are exponential decay function fits of the measured T_1 relaxation curves.

The T_1 -relaxometry measurement protocol is depicted in Figure 2e and summarized here:^{48,53} A laser pulse (5 μ s) is used first to initialize the NV spins in the $m_S = 0$ state, then a MW π pulse is applied to flip the NV spins to $m_S = -1$ state, and finally, a readout laser pulse (5 μ s) is applied after varying measurement time τ . This sequence is followed by the same sequence but without π pulse. This method and physics under it are explained in references [48] and [53]. To optimize the timing, each readout laser pulse is used as an initialization pulse for the next sequence. The NV fluorescence is detected by a sCMOS camera, where exposure (4 ms) starts well before the laser pulse, so that the camera stops reading after the first microsecond of the laser induced fluorescence pulse. The first microsecond contains the ODMR contrast signal, which is maximal when the spins are just initialized into $m_S = -1$ or $m_S = 0$ states but decrease with increasing measurement time τ due to the spin polarization relaxation. We extract this contrast by pixelwise subtracting frames for NVs initialized into $m_S = -1$ (with π pulse) from NVs initialized into $m_S = 0$ state (without π pulse) then dividing them pixelwise by a sum of both frames. The pair of measurements is repeated $N = 10^4$ times for each value of varying time τ (see Figures S6b, S6c, and S6d). Figure 2f shows preliminary measurements of the ODMR contrast vs time τ on bare (filled circles) and Cyt-C drop-casted (open circles) NV sensors from an integrated area of 1296 μm^2 , fitted with one exponential decay function to extract T_1 values (see the Supporting Information Section S6). A reduction of T_1 from ~ 1.2 ms for the bare diamond to 340 μ s after adding 18 μ M Cyt-C is obtained and attributed to the spin-noise originating from iron spins present within the Cyt-C proteins.

To differentiate the effect of Fe^{+3} spins within the Cyt-C nanoclusters from other spin noises due to paramagnetic impurities^{54,55} inside the diamond lattice and the diamond surface noise,⁵⁶ we performed T_1 relaxometry imaging on a nanostructured diamond chip with SiN grating (a separation distance of 4 μm and height of 50 nm). Such a grating is very robust against acids/chemicals during the repeated cleaning process in contrary to other polymers (e.g., polymethyl methacrylate) where they degrade quickly.³⁸ See the Supporting Information Section S4 for the fabrication details. Regions covered with SiN act as barriers for direct dipolar interaction between NV centers and any spin noise on the surface. We found out that the SiN film reduces the Γ_1 rate of NV spins underneath (see Figures 3b and 3f) in comparison to conductive metal (e.g., Al) films where a strong Γ_1 increase was observed.⁵⁷

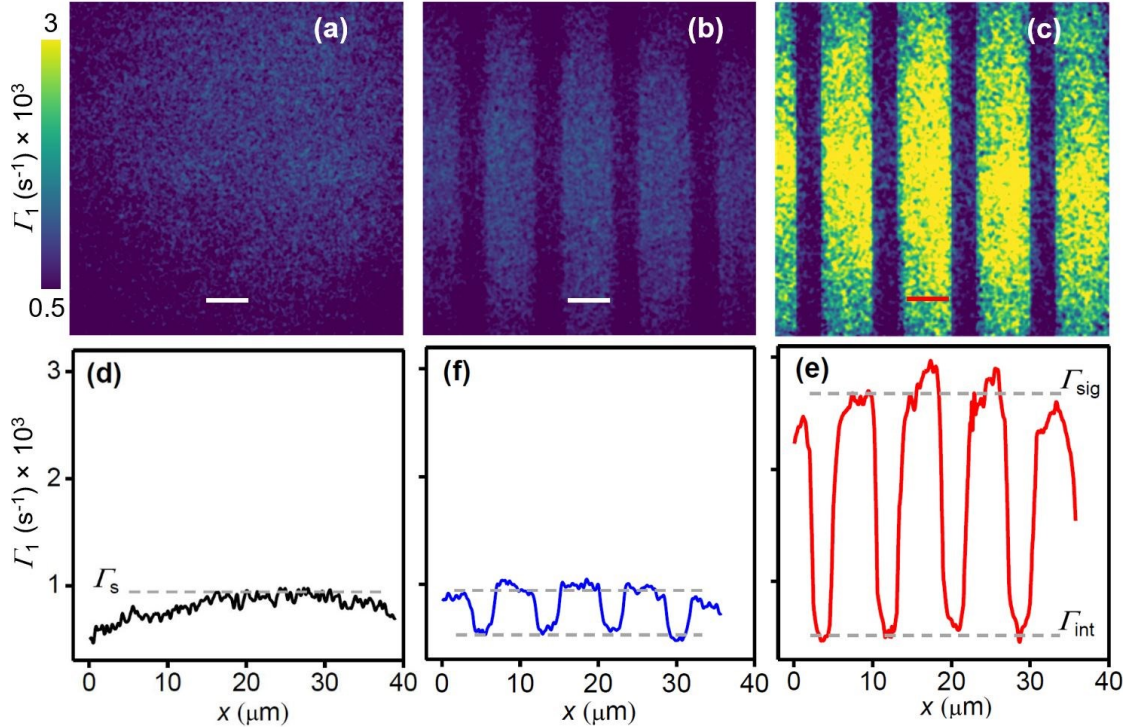


Figure 3. Γ_1 maps acquired by pixelwise exponential fitting of series of maps of the ODMR contrast decays for (a) clean bare diamond, (b) clean diamond with the SiN grating, and (c) Cyt-C with a concentration of 54 μM drop-casted on the diamond with SiN grating. The scale bar in (a), (b), and (c) is 5 μm . Corresponding extracted horizontal Γ_1 profiles from measurements done on bare diamond (d), diamond with SiN grating and no Cyt-C (f), and diamond with SiN and Cyt-C (e), respectively.

Figures 3a, 3b, and 3c show Γ_1 images of the bare diamond, diamond with SiN grating (no Cyt-C), and diamond with SiN and Cyt-C, respectively. The Γ_1 images are obtained from a series of contrast decay images by pixel-by-pixel fitting with a single exponential function. For further analysis, we integrate Γ_1 images vertically to measure the Γ_1 profiles of the measured signals on bare diamond (Figure 3d), diamond with SiN grating and no Cyt-C (Figure 3f), and diamond with SiN and Cyt-C (Figure 3e), simultaneously. The maximum value of $\Gamma_1 = \Gamma_s$ (see Figures 3d and 3f) obtained from uncovered clean areas of the NV sensors is $(0.91 \pm 0.05) \times 10^3 \text{ s}^{-1}$. This value decreases towards the edges of the measurement spot due to a slight drop in the intensity of the laser beam profile, leading to a decrease in the ODMR contrast, which changes the estimation of Γ_1 . To avoid this effect, we estimated the relaxation rates in the central part of the measurement spot, where the laser intensity is relatively homogenous. The relaxation rate $\Gamma_1 = \Gamma_{\text{int}}$ is $(0.45 \pm 0.05) \times 10^3 \text{ s}^{-1}$ under the SiN gratings, which

significantly cancels the surface spin noise of the NV sensor. The relaxation rate $\Gamma_1 = \Gamma_{\text{sig}}$ in the presence of Cyt-C nanoclusters with a concentration of $54 \mu\text{M}$ is $(2.8 \pm 0.2) \times 10^3 \text{ s}^{-1}$ (Figure 3e). Note that the relaxation rate Γ_s of our specific diamond sensor with very shallow NV centers is the sum of the intrinsic relaxation Γ_{int} and the relaxation Γ_{sur} due to surface spin noise, which accounts for almost half of the relaxation of the Γ_s . However, the relaxation rate under presence of Cyt-C analyte is $\Gamma_{\text{sig}} = \Gamma_{\text{int}} + \Gamma_{\text{sur}} + \Gamma_{\text{ext}}$. From the measurements with very low concentrations of Cyt-C proteins (Figure 4d), we found that the Γ_{sur} is significantly suppressed also by the dilute solution and could be neglected, so that $\Gamma_{\text{ext}} \approx \Gamma_{\text{sig}} - \Gamma_{\text{int}}$.

Cyt-C proteins, having Fe^{+3} centers, produce fluctuating magnetic fields that interact with NV spins via dipolar-magnetic-interactions.^{37,38,50,58} Figures 4a, 4b, and 4c show the Γ_1 images of Cyt-C solution drop-casted onto the diamond substrate with three concentrations of $25 \mu\text{M}$, $18 \mu\text{M}$, and $11 \mu\text{M}$, respectively. Figure 4d displays the measured relaxation rate Γ_{ext} (open circles) as a function of the number of Fe^{+3} centers adsorbed per μm^2 . We calculated the theoretical dependence of the relaxation rates vs the density of Fe^{+3} adsorbed centers per $1 \mu\text{m}^2$ (solid line in Figure 4d) by using Equation S1 and keeping the dipolar interaction field between NV and Cyt-C $\langle B^2 \rangle$ as a free parameter (see the Supporting Information Section S8). For a spin density of 1.7×10^7 Fe adsorbed/ μm^2 we determined $\langle B^2 \rangle$ of the Fe spins in Cyt-C to be 0.084 mT .

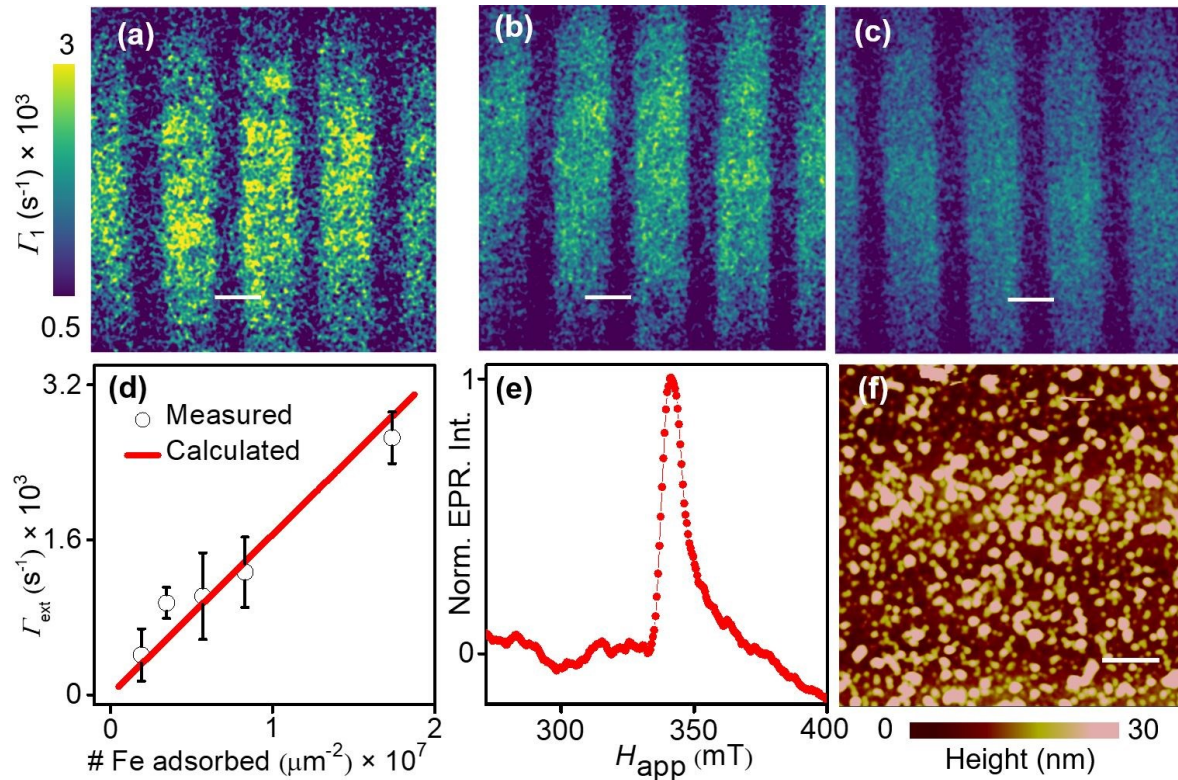


Figure 4. (a) NV Γ_1 map of Cyt-C nanoclusters drop-casted on diamond with a concentration of $25 \mu\text{M}$. The bright regions marked the increased relaxation rate due in presence of Cyt-C in contact (no SiN grating) with diamond. The dark regions have SiN due to which the relaxation rate of NV spins gets unaffected. The scale bar is $5 \mu\text{m}$. (b) and (c) are the Γ_1 maps in the presence of $18 \mu\text{M}$ and $11 \mu\text{M}$ drop-casted Cyt-C nanoclusters, respectively. (d) Measured (open circles) and calculated (solid line) relaxation rate $\Gamma_1 = \Gamma_{\text{ext}}$ of NV spins as function of the density of Fe spins adsorbed on the diamond substrate over $1 \mu\text{m}^2$ area. (e) Measured EPR spectrum of pelletized 15 mg Cyt-C powder. (f) AFM image ($30 \mu\text{m} \times 30 \mu\text{m}$) taken on diamond with Cyt-C nanoclusters with a concentration of $54 \mu\text{M}$. The AFM image shows the uniform adsorption of Cyt-C proteins on the diamond surface.

EPR spectroscopy is employed to determine the g -factor of Fe^{+3} present in Cyt-C proteins and their fluctuations rate by analyzing the linewidth parameter of the EPR signal, as illustrated in Figure S7. We deduced an EPR full width at half maximum (FWHM) of 71.43 mT for the pelletized 15 mg Cyt-C powder, corresponding to a fluctuation rate of Fe^{+3} spins in Cyt-C of ~ 2 GHz.³⁸ We also used AFM imaging as an additional method to estimate the Fe^{+3} spin density within Cyt-C molecules, similar to the approach used in reference [50] to determine the adsorbed Fe^{+3} on the diamond surface. Figure 4f shows the AFM image of $30\ \mu\text{m} \times 30\ \mu\text{m}$ area of Cyt-C nanoclusters at a concentration of $54\ \mu\text{M}$, drop-casted on the functionalized diamond surface (see Figure 3c for the corresponding T_1 image). By measuring the diameter and height of Cyt-C nanoclusters from the AFM image one can obtain the volume and therefore the concentration of the drop-casted Cyt-C molecules. For instance, $4\ \mu\text{L}$ of $54\ \mu\text{M}$ Cyt-C is drop-casted on the diamond surface (Figure 4f) for which we obtain a spin density of $\sim 1.7 \times 10^7$ adsorbed $\text{Fe}/\mu\text{m}^2$. This value agrees well with the calculated Fe^{+3} spin density value based on the NV imaged area of Cyt-C nanoclusters ($36 \times 36\ \mu\text{m}$).

In conclusion, we demonstrate the detection of Fe spins in nanoclustered (diameter: 50 – 200 nm, height: 5 – 15 nm) Cyt-C proteins, extracted from horse heart, by using NV T_1 relaxometry in combination with EPR spectroscopy and AFM imaging techniques. NV T_1 relaxometry allows the detection of spin-noise generated by Fe^{+3} spins present in Cyt-C proteins via the reduction of T_1 . By patterning the diamond with SiN grating, we perform relaxometry imaging of nanoclustered Cyt-C proteins with different concentrations. The measured NV relaxation rates agree well with the calculated values deduced from a model of interacting Fe^{+3} centers with NV spins in the diamond substrate with a standoff 5.5 nm. These results open the door to detect Fe in Cyt-C on surface-immobilized microbial cells, with the goal of elucidating the effects of Fe, both in ferrous (Fe^{+2}) and ferric (Fe^{+3}) states, on the electron transport processes during metabolism. The integration of microfluidics³⁸ and environment control (e.g., no oxygen) to NV magnetometry may allow measuring Cyt-C in many microbes such as *M. sedula*, *R. palustris*, and *M. acetivorans* under aerobic and anaerobic conditions.

Combining NV- T_1 magnetic relaxometry with NV-NMR^{33–36} and NV-EPR⁵⁹ may enable analyzing Cyt-C inside cells (in vivo) or at least in the cell lysates (in vitro) by distinguishing the different spin signatures. Cyt-C is released from the mitochondria into the cytoplasm of the cell during apoptosis (e.g., hepatocytes). Cytoplasmic release of Cyt-C, a mitochondrial electron transporter, is a prominent indicator of such critical steps. Therefore, visualizing Cyt-C efflux in living cells is a convenient approach to address apoptosis triggering and monitor performance of apoptosis restoration strategies.⁶⁰ Using nanodiamonds with longer NV spin relaxation (T_1) and spin coherence (T_2) times,⁶¹ functionalized with cells containing Cyt-C, may enable detection of intracellular Fe concentrations.

ASSOCIATED CONTENT

Supporting Information

SEM measurements to confirm the diameter of the Cyt-C nanoclusters, XPS analysis, functionalization of the diamond surface, fabrication of the SiN grating, creation of NV centers in diamond and optical detected magnetic resonance setup, NV magnetic relaxometry imaging, EPR analysis, and theoretical estimation of relaxation rate of NV spins. This material is available free of charge via the Internet at <http://pubs.acs.org>.

AUTHOR INFORMATION

Corresponding Author

* Abdelghani Laraoui, E-mail: alaraoui2@unl.edu

Author Contributions

S.L. and R.T. performed NV measurements. C.S. synthesized the cytochrome C powder and functionalized the diamond surface. S.L. performed XPS, AFM, and SEM. I.F and A.L developed the NV-T1 relaxometry imaging technique. I.F. helped in analyzing and fitting the measured relaxometry images. K.A. performed EPR measurements. S.-H.L, R.Y.L., and A.L. conceived the cytochrome C study and supervised the project. All authors discussed the results. A.L wrote the manuscript with contributions of all authors.

ACKNOWLEDGMENTS

This material is based upon work supported by the NSF/EPSCoR RII Track-1: Emergent Quantum Materials and Technologies (EQUATE) Award OIA-2044049, and NSF Award 2328822. I.F. acknowledges support from Latvian Council of Science project lzp- 2021/1-0379. K.A. would like to acknowledge the support of the National Science Foundation/EPSCoR RII Track-4 Award OIA-2033210 and NSF Award 2328822. The research was performed in part in the Nebraska Nanoscale Facility: National Nanotechnology Coordinated Infrastructure and the Nebraska Center for Materials and Nanoscience (and/or NERCF), which are supported by NSF under Award ECCS: 2025298, and the Nebraska Research Initiative. We thank V.M. Acosta for suggesting the fabrication of non-metallic grating on diamond to prevent quenching effects caused by metals.

Supporting Information

S1. Scanning electron microscopy analysis (SEM) of cytochrome C nanoclusters

Figure S1a shows the SEM image performed on cytochrome C (Cyt-C) of 2 μM drop-casted on the diamond substrate. To prevent charging issues, we sputtered the diamond substrate with Cyt-C with an ultrathin (thickness of 2.5 ± 0.5 nm) layer of Au. The diameter distribution of the Cyt-C nanoclusters is illustrated in the histogram depicted in Figure S1b indicating a mean diameter of $\sim 100 \pm 50$ nm. The diameter is still way higher than the transmission electron microscopy (TEM) measured one (3.4 nm) in reference [44], indicating that the aggregation is still occurring.

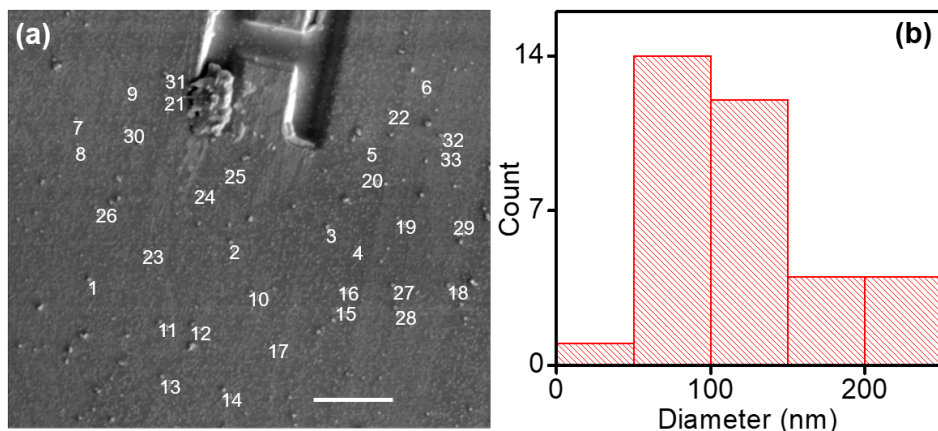


Figure S1. (a) SEM image of Cyt-C (concentration of 2 μM) drop-casted on the diamond chip and coated with $\sim 2.5 \pm 0.5$ nm Au film to prevent charging effect. (b) The diameter distribution of Cyt-C nanoclusters with a diameter of 100 ± 50 nm.

S2. X-ray photoelectron spectroscopy (XPS)

We drop-casted 5 μL solution containing 54 μM concentration of Cyt-C onto a silicon substrate, allowing it to evaporate and form a thin film. Subsequently, X-ray photoelectron spectroscopy (XPS) analysis was conducted using Thermo Scientific Al K-Alpha XPS system, which operated under ultrahigh vacuum conditions at a pressure of 1×10^{-9} mbar. Data acquisition and analysis were performed using the AvantageTM software package. To compensate for charge effects during measurement, a combination of electron and argon ion flood guns was employed, maintaining an argon pressure in the chamber ranging from 2×10^{-8} to 4×10^{-8} mbar. The X-ray beam had a diameter of 400 μm , and high-energy resolution spectra were recorded with a pass energy of 50 eV, utilizing a step size of 0.1 eV and a dwell time of 50 ms respectively. The number of averaged sweeps for each element was adjusted to optimize the signal to noise ratio, typically ranging from 20 to 100 sweeps.

For data analysis, we calibrated all spectra relative to a carbon 1s (Figure S2a) peak positioned at 284.8 eV to correct for any charging effects. Additionally, we performed background correction using the smart background subtraction feature within the AvantageTM package. Spectral analysis involved peak deconvolution, which utilized a combination of Gaussian and Lorentzian functions. The XPS results obtained for N 1s, O 1s, and S 2p are plotted in Figures S2b, S2c, and S2d. In the context of S 2p spectroscopy, we observe two distinct peaks. The first peak appears at 163.4 eV, indicating the presence of Fe-S bonding. This peak corresponds to the spectral line associated with the $2p_{1/2}$ electron configuration. The second peak occurring at 167 eV is associated with the spectral line of $2p_{3/2}$. This peak signifies the presence of sulfur bonded to the carbon-oxygen (C-O) chain.⁶²

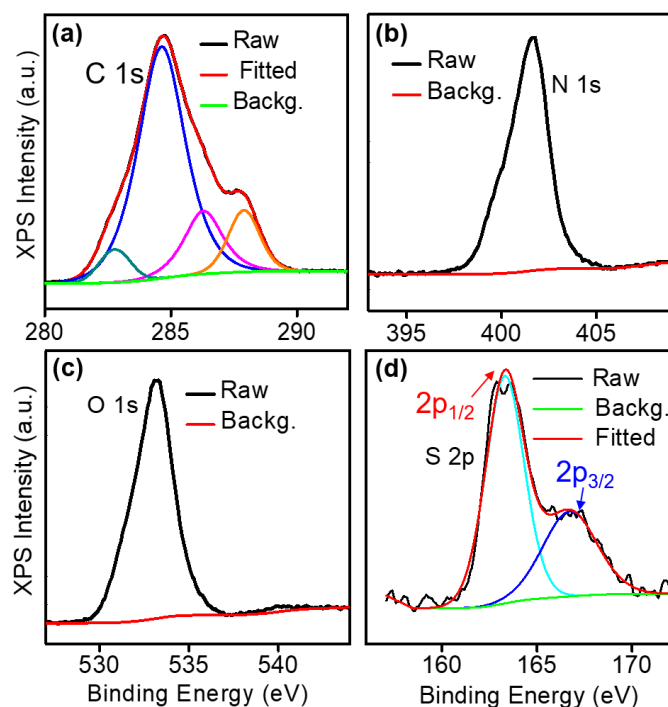


Figure S2. High resolution XPS peak with the background for (a) C 1s, (b) N 1s, (c) O 1s, and (d) S 2p. The deconvoluted analysis for S 2p is also shown. There are two peak positions at 163 eV and 167 eV. 167 eV corresponds to the Fe-S binding energy.

S3. Functionalization of the diamond substrate.

To attach Cyt-C proteins, the NV-doped diamond chip was carboxylated at room temperature in a 9:1 mixture of concentrated $\text{H}_2\text{SO}_4:\text{HNO}_3$ for 72 hours. The diamond substrate was then rinsed and treated with 0.1 M HCl at 90 °C for 2 hours, followed by 0.1 M NaOH at 90 °C for 2 hours. The modification was confirmed using a Nicolet AVATAR 380 Fourier-transform infrared spectroscopy (FTIR) between 1000 cm^{-1} to 3000 cm^{-1} . Peaks at 1960 cm^{-1} , 2030 cm^{-1} , 2160 cm^{-1} , and 2500 cm^{-1} in the carboxylated diamond substrate are the intrinsic signature peaks for the diamond, Figure S3a. The two peaks at 2850 cm^{-1} and 2920 cm^{-1} showed an increase in hydrogen absorption on the surface. This facilitates the attachment of the Cyt-C molecules to the diamond surface. Figure S3b shows the T_1 relaxation measurement curves of the diamond before (filled circles) and after (open circles) the functionalization process. T_1 value is obtained as $1.24 \pm 0.1\text{ ms}$ and $1.16 \pm 0.094\text{ ms}$ before and after functionalization, respectively. The slight change in T_1 is related to the measurements done on a different region before and after carboxylation as there is a slight spatial change of the NV density, read the Supporting Information Section S5.

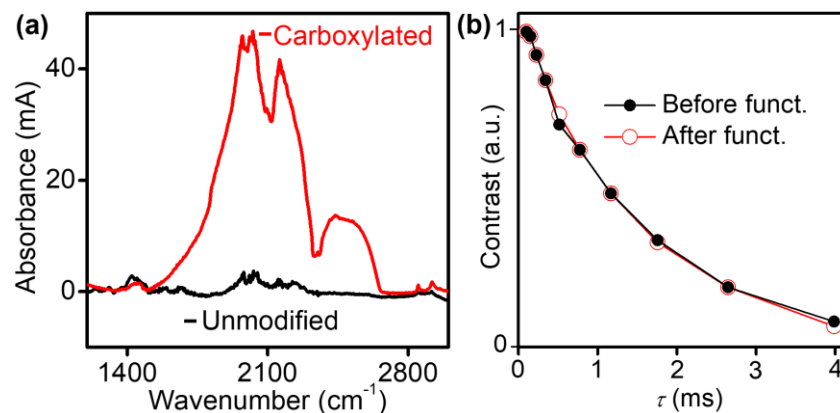


Figure S3. (a) FTIR spectroscopy of diamond chip before (red solid line) and after (black solid line) the functionalization of the diamond substrate. (b) T_1 relaxation of the diamond chip before (scattered filled-circle line) and after (scattered open-circle line) functionalization showing a slight change in relaxation times T_1 with the surface treatment.

S4. Nanofabrication of SiN grating on top of diamond

We employed the lift-off technique to fabricate the grating structure on $4\text{ mm} \times 4\text{ mm} \times 0.5\text{ mm}$ diamond substrate. The diamond chip underwent a cleaning process involving a $200\text{ }^\circ\text{C}$ treatment with tri-acid for a duration of 2 hours. Subsequently, a spin-coating process was utilized to apply a layer of LOR-3A, followed by the deposition of AZ-3312, which is a positive photoresist. To define the grating pattern, we utilized the Heidelberg DWL 66FS Laser Lithography system to expose the photoresist. After exposure, a development step was performed. To refine the surface, an ion beam milling process was employed to etch the 10 nm thick layer.

Following this, a 50 nm layer of silicon nitride (SiN) was sputter-deposited onto the substrate. The final step involved cleaning the diamond substrate to remove all the photoresist and the diamond with grating was subsequently cleaned in tri acid mixture at $200\text{ }^\circ\text{C}$. The dimension of SiN grid is $4\text{ }\mu\text{m}$ in width followed by a separation of $4\text{ }\mu\text{m}$ between the grids. Figure S4a shows the optical image of the grating on diamond with photoresist after DWL exposure and development. Figure S4b represents the AFM image of zoomed $20\text{ }\mu\text{m}$ by $20\text{ }\mu\text{m}$ grating, confirming the grating height of $50 \pm 5\text{ nm}$.

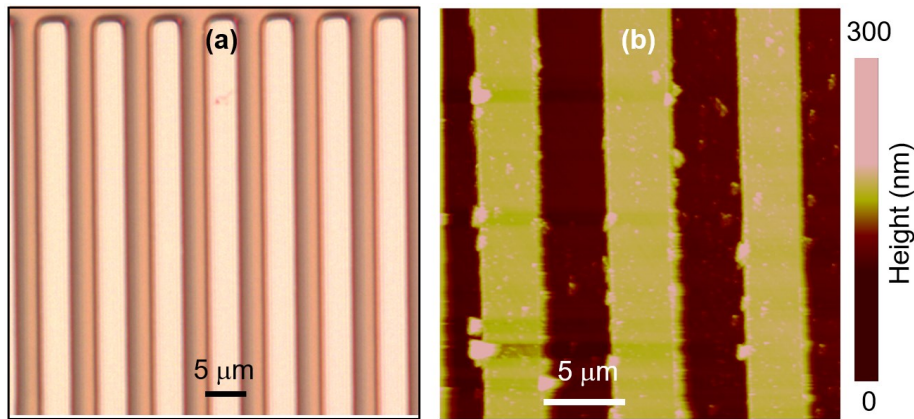


Figure S4. (a) Optical image of the SiN grating made on top of the diamond substrate after exposure with laser and development. (b) Zoomed AFM scan of the SiN grating with Cyt-C nanoclusters.

S5. Experimental setup: optical detected magnetic resonance

Creation of nitrogen vacancy (NV) centers in diamond. We used $4\text{ mm} \times 4\text{ mm} \times 0.5\text{ mm}$ type-IIa electronic grade (100) diamond (Element Six) substrate with a nitrogen concentration of < 5 ppb. We made first the SiN grating (Supporting Information Section S4) and then cut and polished the diamond substrate along the (100) plane at Delaware Diamond Knives, Inc. to obtain $4\text{ mm} \times 2.5\text{ mm} \times 0.05\text{ mm}$ membranes. The diamond is then implanted at CuttingEdge Ions with $^{15}\text{N}^+$ ions at an energy of 4 keV and a dose of $1 \times 10^{13}\text{ cm}^{-2}$ respectively to create a uniform layer of vacancies near the diamond surface $\sim 5 - 8\text{ nm}$.^{22,51} We used Stopping and Range of Ions in Matter (SRIM) Monte Carlo simulations to estimate the vacancy distribution depth profile in the diamond and found a uniform distribution within $\sim 8\text{ nm}$ beneath the diamond surface facing the $^{15}\text{N}^+$ source, Figure S5a. After the implantation we annealed the diamond substrate in an high vacuum (pressure $\leq 10^{-6}$ torr) furnace at $850\text{ }^\circ\text{C}$ for 4 hours and at $1100\text{ }^\circ\text{C}$ for 2 hours, and then cleaned it for two hours in a 1:1:1 mixture of nitric, sulfuric, and perchloric acid at $200\text{ }^\circ\text{C}$ to remove graphite residues at the surface.^{22,35,51} This process resulted in $\sim 5 - 8\text{ nm}$ NV layer near the surface with a density of ~ 1 ppm, based on the fluorescence measurements.⁶³

Optical detected magnetic resonance setup. The wide field microscope (WFM) used in this study is a home-built optical detected magnetic resonance (ODMR) setup combined with sCMOS camera for wide-field imaging.^{17,29} We used an oil immersion $100\times$ Nikon objective with a

working distance of 0.23 mm and NA of 1.25 to focus the pulsed green laser (532 nm) with a variable laser power (up to 2 W). The green laser pulsing is done by using Acousto-optical modulator (AOM) TEM-200-50-532 (Brimrose) and taking only the first order of diffraction laser mode. The carboxylated diamond substrate with 50-nm thick SiN grating and drop-casted Cyt-C is attached to a glass coverslip (thickness of 100 μm) with one microwave (MW) Au loop patterned on it for NV spin excitation. The coverslip with diamond is then mounted on a x - y - z motorized stage (Newport, Picometer 8742) that is connected to the computer through a USB interface for imaging a selected region of the sample. The fluorescence (650 – 800 nm) is collected by the same objective, transmitted through a dichroic mirror (DM, Semrock model #FF560-FDi01) and a single-band bandpass filter (Semrock FF01-731-137), and then focused on the sCMOS camera (Hamamatsu, ORCA-Flash4.0 V3) via a tube lens (Thorlabs, TTL200). For magnetic field alignment, the NV fluorescence is reflected by a flip mirror and focused with a lens (focal length of 30 mm) on an avalanche photon detector (APD, Thorlabs APD410A), connected to a Yokogawa oscilloscope (DL9041L). More details of the setup can be found in reference [17].

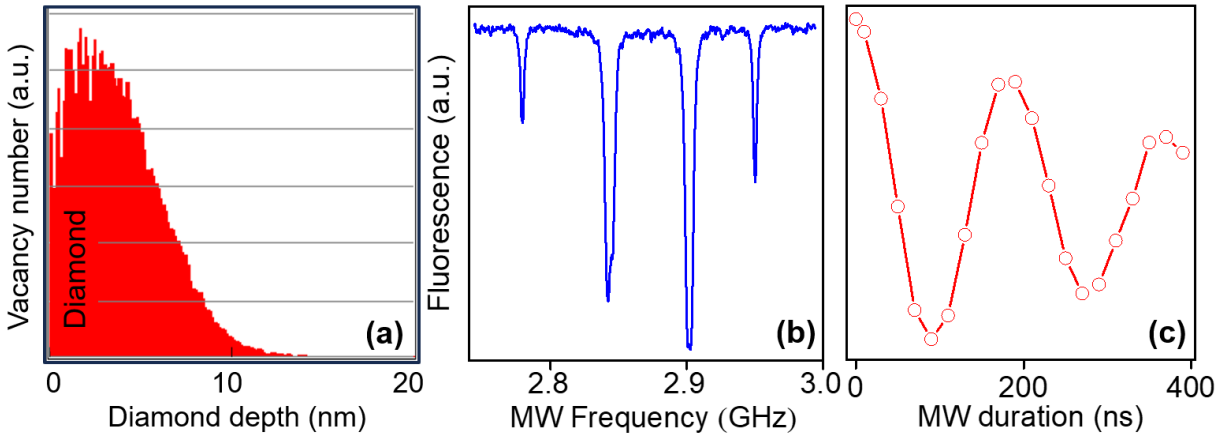


Figure S5. (a) Vacancy distribution obtained from SRIM calculations for 4 keV implanted ^{15}N in diamond (carbon) substrate. (b) ODMR spectrum of the diamond at B_{app} of 3.2 mT. (c) Rabi oscillations of $m_S = 0$ to $m_S = -1$ spin transition at a MW frequency 2.78 GHz.

To perform pulsed (Rabi and T_1) NV measurements, we used a 400 MHz Pulse Blaster card (Spincore PBESR-PRO-400) to control the timing of green laser/MW pulses with the trigger of sCMOS camera for NV fluorescence detection/imaging. The MW pulses were generated by injecting MW AC current from a signal generator (SRS: Stanford Research Systems, model SG384) and directing it to a solid-state switch (Mini-Circuits ZASWA-2-50DR+), which was electrically operated by the TTL pulse provided by the pulse Blaster. Subsequently, these MW pulses were amplified using a Mini-Circuits ZHL-16W-43-s+ amplifier. We used permanent magnets (KJ magnetics, DX8X8-N52) to apply the magnetic field B_{app} (up to 60 mT) along the NV [111] axis in the (100) diamond. By monitoring the ODMR peaks in the oscilloscope along [111] direction, we can align the applied magnetic field very accurately. **Figure S5b** shows four (two along [111] direction and two of the other merged NV peaks) ODMR peaks for $m_S = 0$ to $m_S = -1$ and $m_S = 0$ to $m_S = +1$ at B_{app} of 3.2 mT. After the magnetic field alignment, we performed Rabi oscillations measurement of the $m_S = 0$ to $m_S = -1$ spins aligned along B_{app} (3.2 mT) to obtain the π -pulse width, needed for T_1 measurement/imaging. The silver mirror was then flipped down to perform NV T_1 relaxometry imaging by the sCMOS camera, by varying the dark time τ .²² Read the main text for further details.

S6. Data acquisition for T_1 relaxometry imaging

We used the following parameters for the camera: frame size is 550 pixels \times 550 pixels (1 pixel = 65 nm at 100 \times magnification), the field of view is 36 μm \times 36 μm . Contrast images were collected at various time τ points and averaged over many cycles ($N = 10^4$) at each τ point. The single τ point images are shown in Figures S6b, S6c and S6d taken at τ of 50 μs , 300 μs and 1000 μs , respectively for a Cyt-C molecule of 18 μM drop-casted on the top of the diamond surface. The presence of Fe^{+3} in Cyt-C generates spin noise, leading to a reduction in the T_1 relaxation time to 346 μs . Figure S3a depicts a decay curve, which was derived by assessing the average contrast from images captured at specific fixed time τ values which was then fitted with an exponential decay curve keeping the amplitude and offset as free parameters to obtain the T_1 relaxation time.

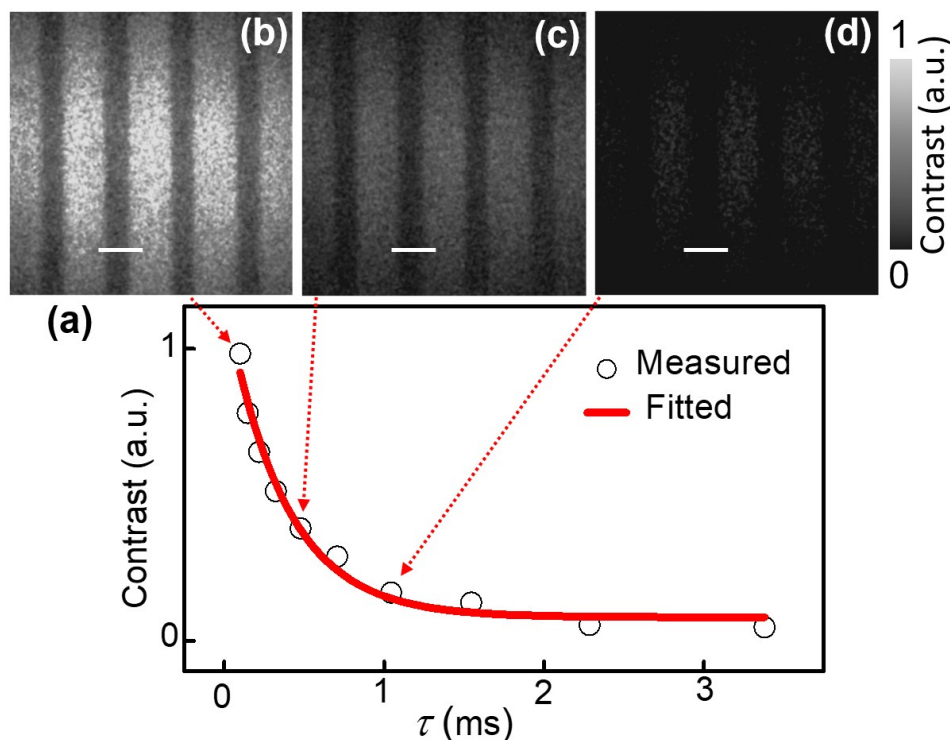


Figure S6. (a) Relaxation measurement (open circles) of NV spins in the presence of Cyt-C nanoclusters with a concentration of 18 μM , fitted (red solid line) with a decay exponential function. (b), (c), and (d) show the single point τ imaging at intervals of 50 μs , 300 μs , and 1000 μs respectively. The scale bar in (b), (c), and (d) is 5 μm .

S7. EPR data analysis.

At room temperature, electron paramagnetic resonance (EPR) measurements were conducted using a Bruker EMX electron spin resonance setup equipped with an X-band metal cavity resonator (ER 4102ST cavity). The measurement conditions involved applying a 2 mT modulation magnetic field at a frequency of 100 kHz, while the MW frequency and power were set to 9.736 GHz and 20 mW respectively. EPR spectroscopy was employed to determine the g -factor of Fe^{+3} spins present in Cyt-C proteins and their dipolar interactions strength by analyzing the linewidth parameter of the EPR signal, as illustrated in **Figure S7**. By examining the first derivative EPR spectrum on pelletized powder Cyt-C (15 mg), we determined a full width at half maximum (FWHM) of 71.43 mT, corresponding to a fluctuation rate of Fe spins in Cyt-C of ~ 2 GHz.³⁸

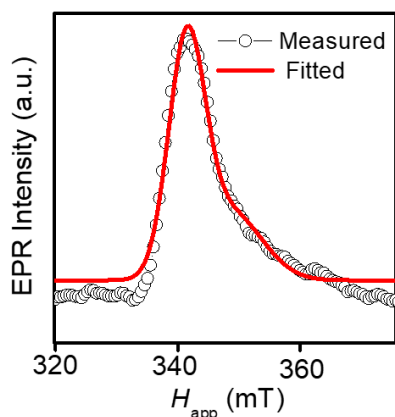


Figure S7. First order EPR spectrum of pelletized Cyt-C powder fitted with Gaussian functions to extract FWHM.

S8. Theoretical estimation of relaxation rate of NV spins

The heme center of Cyt-C produces a fluctuating magnetic field (or spin noise) that interacts with NV spins and reduces its T_1 relaxation time. The relaxation rate $\Gamma_1 = 1/T_1$ is known to be dependent upon (i) the dipolar interaction between external spins (Fe^{+3} for our case) and NV spins and (ii) the fluctuation rate of the Fe^{+3} spins.³⁷ This phenomenon is explained with the equation:³⁷

$$\Gamma_1 = \frac{2\langle B^2 \rangle f_t}{f_t + D^2}, \quad (\text{Eq. 1})$$

where, f_t is the fluctuation rate of external spins, $\langle B^2 \rangle$ is the mean dipolar magnetic coupling strength between the NV spins and the external Fe^{+3} spins, and D is zero field splitting of the NV spin ground state ~ 2.87 GHz. To calibrate our measurements and deduce the NV standoff d , we measured the relaxation rate Γ_1 in CuSO_4 solutions of different concentrations on the diamond substrate. We used equation Eq.1 to estimate the theoretical relaxation rate of copper ions, Figure S8. The relaxation rate of the copper ions was used as 0.3 GHz^{38} and the dipolar magnetic field as a function of NV standoff (d) and concentration (c) is given as:³⁸

$$10^3 \times \frac{\pi c N_A}{8d^3} \times \left(\frac{\mu_0}{4\pi h} g_{NV} g_s \mu_B^2 \right)^2, \quad (\text{Eq. 2})$$

where g_{NV} and g_s are the gyromagnetic ratio for NV spins and Cu ions respectively. N_A , μ_B and h are Avogadro's number, Bohr magneton, and Planck's constant respectively. The NV standoff was kept as a free parameter to match the fitting. As a result, we get the NV standoff of 5.5 nm.

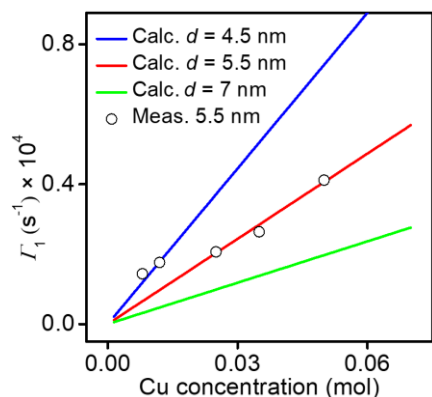


Figure S8. Relaxation rate Γ_1 vs the concentration of Cu ions obtained both experimentally (open circles) and theoretically (solid lines: green: $d = 7$ nm; red: $d = 5.5$ nm; and blue: $d = 4.5$ nm).

REFERENCES

- (1) Bertini, I.; Cavallaro, G.; Rosato, A. Cytochrome *c*: Occurrence and Functions. *Chem. Rev.* **2006**, *106* (1), 90–115. <https://doi.org/10.1021/cr050241v>.

- (2) Ow, Y.-L. P.; Green, D. R.; Hao, Z.; Mak, T. W. Cytochrome c: Functions beyond Respiration. *Nat Rev Mol Cell Biol* **2008**, *9* (7), 532–542. <https://doi.org/10.1038/nrm2434>.
- (3) Liu, J.; Chakraborty, S.; Hosseinzadeh, P.; Yu, Y.; Tian, S.; Petrik, I.; Bhagi, A.; Lu, Y. Metalloproteins Containing Cytochrome, Iron–Sulfur, or Copper Redox Centers. *Chem. Rev.* **2014**, *114* (8), 4366–4469. <https://doi.org/10.1021/cr400479b>.
- (4) Kühlbrandt, W. Structure and Function of Mitochondrial Membrane Protein Complexes. *BMC Biol* **2015**, *13* (1), 89. <https://doi.org/10.1186/s12915-015-0201-x>.
- (5) Eleftheriadis, T.; Pissas, G.; Liakopoulos, V.; Stefanidis, I. Cytochrome c as a Potentially Clinical Useful Marker of Mitochondrial and Cellular Damage. *Front. Immunol.* **2016**, *7*. <https://doi.org/10.3389/fimmu.2016.00279>.
- (6) Li, P.; Nijhawan, D.; Budihardjo, I.; Srinivasula, S. M.; Ahmad, M.; Alnemri, E. S.; Wang, X. Cytochrome c and dATP-Dependent Formation of Apaf-1/Caspase-9 Complex Initiates an Apoptotic Protease Cascade. *Cell* **1997**, *91* (4), 479–489. [https://doi.org/10.1016/S0092-8674\(00\)80434-1](https://doi.org/10.1016/S0092-8674(00)80434-1).
- (7) Radhakrishnan, J.; Wang, S.; Ayoub, I. M.; Kolarova, J. D.; Levine, R. F.; Gazmuri, R. J. Circulating Levels of Cytochrome c after Resuscitation from Cardiac Arrest: A Marker of Mitochondrial Injury and Predictor of Survival. *American Journal of Physiology-Heart and Circulatory Physiology* **2007**, *292* (2), H767–H775. <https://doi.org/10.1152/ajpheart.00468.2006>.
- (8) Zager, R. A.; Johnson, A. C. M.; Hanson, S. Y. Proximal Tubular Cytochrome c Efflux: Determinant, and Potential Marker, of Mitochondrial Injury. *Kidney International* **2004**, *65* (6), 2123–2134. <https://doi.org/10.1111/j.1523-1755.2004.00638.x>.
- (9) Zheng, N.; Wang, T.; Wei, A.; Chen, W.; Zhao, C.; Li, H.; Wang, L. High-content Analysis Boosts Identification of the Initial Cause of Triptolide-induced Hepatotoxicity. *J of Applied Toxicology* **2019**, *39* (9), 1337–1347. <https://doi.org/10.1002/jat.3821>.
- (10) Picklo, M. J.; Zhang, J.; Nguyen, V. Q.; Graham, D. G.; Montine, T. J. High-Pressure Liquid Chromatography Quantitation of Cytochrome c Using 393 Nm Detection. *Analytical Biochemistry* **1999**, *276* (2), 166–170. <https://doi.org/10.1006/abio.1999.4349>.
- (11) Bachhav, Y. G.; Kalia, Y. N. Development and Validation of an Analytical Method for the Quantification of Cytochrome c in Skin Transport Studies. *Biomed. Chromatogr.* **2009**, *24* (7), 732–736. <https://doi.org/10.1002/bmc.1356>.
- (12) Pyka, J.; Osyczka, A.; Turyna, B.; Blicharski, W.; Froncisz, W. EPR Studies of Iso-1-Cytochrome c : Effect of Temperature on Two-Component Spectra of Spin Label Attached to Cysteine at Positions 102 and 47. *European Biophysics Journal* **2001**, *30* (5), 367–373. <https://doi.org/10.1007/s002490100168>.
- (13) Van Son, M.; Schilder, J. T.; Di Savino, A.; Blok, A.; Ubbink, M.; Huber, M. The Transient Complex of Cytochrome c and Cytochrome c Peroxidase: Insights into the Encounter Complex from Multifrequency EPR and NMR Spectroscopy. *ChemPhysChem* **2020**, *21* (10), 1060–1069. <https://doi.org/10.1002/cphc.201901160>.
- (14) Blum, H.; Ohnishi, T. Electron Spin Relaxation of the Electron Paramagnetic Resonance Spectra of Cytochrome c. *Biochimica et Biophysica Acta (BBA) - Protein Structure* **1980**, *621* (1), 9–18. [https://doi.org/10.1016/0005-2795\(80\)90057-4](https://doi.org/10.1016/0005-2795(80)90057-4).
- (15) Ichimura, K.; Nakahara, Y.; Kimura, K.; Inokuchi, H. Electronic States of Oxidized and Reduced Cytochrome c Observed by X-Ray Photoelectron Spectroscopy. *J. Mater. Chem.* **1992**, *2* (11), 1185. <https://doi.org/10.1039/jm9920201185>.
- (16) Stavis, C.; Clare, T. L.; Butler, J. E.; Radadia, A. D.; Carr, R.; Zeng, H.; King, W. P.; Carlisle, J. A.; Aksimentiev, A.; Bashir, R.; Hamers, R. J. Surface Functionalization of Thin-Film Diamond for Highly Stable and Selective Biological Interfaces. *Proc. Natl. Acad. Sci. U.S.A.* **2011**, *108* (3), 983–988. <https://doi.org/10.1073/pnas.1006660107>.
- (17) Lamichhane, S.; McElveen, K. A.; Erickson, A.; Fescenko, I.; Sun, S.; Timalsina, R.; Guo, Y.; Liou, S.-H.; Lai, R. Y.; Laraoui, A. Nitrogen-Vacancy Magnetometry of Individual Fe-Triazole Spin Crossover Nanorods. *ACS Nano* **2023**, *17* (9), 8694–8704. <https://doi.org/10.1021/acsnano.3c01819>.

- (18) De Gille, R. W.; McCoe, J. M.; Hall, L. T.; Tetienne, J.-P.; Malkemper, E. P.; Keays, D. A.; Hollenberg, L. C. L.; Simpson, D. A. Quantum Magnetic Imaging of Iron Organelles within the Pigeon Cochlea. *Proc. Natl. Acad. Sci. U.S.A.* **2021**, *118* (47), e2112749118. <https://doi.org/10.1073/pnas.2112749118>.
- (19) McCoe, J. M.; Matsuoka, M.; De Gille, R. W.; Hall, L. T.; Shaw, J. A.; Tetienne, J.; Kisailus, D.; Hollenberg, L. C. L.; Simpson, D. A. Quantum Magnetic Imaging of Iron Biomineralization in Teeth of the Chiton *Acanthopleura Hirtosa*. *Small Methods* **2020**, *4* (3), 1900754. <https://doi.org/10.1002/smt.201900754>.
- (20) Schäfer-Nolte, E.; Schlipf, L.; Ternes, M.; Reinhard, F.; Kern, K.; Wrachtrup, J. Tracking Temperature-Dependent Relaxation Times of Ferritin Nanomagnets with a Wideband Quantum Spectrometer. *Phys. Rev. Lett.* **2014**, *113* (21), 217204. <https://doi.org/10.1103/PhysRevLett.113.217204>.
- (21) Wang, P.; Chen, S.; Guo, M.; Peng, S.; Wang, M.; Chen, M.; Ma, W.; Zhang, R.; Su, J.; Rong, X.; Shi, F.; Xu, T.; Du, J. Nanoscale Magnetic Imaging of Ferritins in a Single Cell. *Sci. Adv.* **2019**, *5* (4), eaau8038. <https://doi.org/10.1126/sciadv.aau8038>.
- (22) Fescenko, I.; Laraoui, A.; Smits, J.; Mosavian, N.; Kehayias, P.; Seto, J.; Bougas, L.; Jarmola, A.; Acosta, V. M. Diamond Magnetic Microscopy of Malarial Hemozoin Nanocrystals. *Phys. Rev. Applied* **2019**, *11* (3), 034029. <https://doi.org/10.1103/PhysRevApplied.11.034029>.
- (23) Doherty, M. W.; Manson, N. B.; Delaney, P.; Jelezko, F.; Wrachtrup, J.; Hollenberg, L. C. L. The Nitrogen-Vacancy Colour Centre in Diamond. *Physics Reports* **2013**, *528* (1), 1–45. <https://doi.org/10.1016/j.physrep.2013.02.001>.
- (24) Laraoui, A.; Dolde, F.; Burk, C.; Reinhard, F.; Wrachtrup, J.; Meriles, C. A. High-Resolution Correlation Spectroscopy of ¹³C Spins near a Nitrogen-Vacancy Centre in Diamond. *Nat Commun* **2013**, *4* (1), 1651. <https://doi.org/10.1038/ncomms2685>.
- (25) Laraoui, A.; Hodges, J. S.; Meriles, C. A. Magnetometry of Random AC Magnetic Fields Using a Single Nitrogen-Vacancy Center. *Appl. Phys. Lett.* **2010**, *97* (14), 143104. <https://doi.org/10.1063/1.3497004>.
- (26) Balasubramanian, G.; Neumann, P.; Twitchen, D.; Markham, M.; Kolesov, R.; Mizuochi, N.; Isoya, J.; Achard, J.; Beck, J.; Tissler, J.; Jacques, V.; Hemmer, P. R.; Jelezko, F.; Wrachtrup, J. Ultralong Spin Coherence Time in Isotopically Engineered Diamond. *Nature Mater* **2009**, *8* (5), 383–387. <https://doi.org/10.1038/nmat2420>.
- (27) Degen, C. L.; Reinhard, F.; Cappellaro, P. Quantum Sensing. *Rev. Mod. Phys.* **2017**, *89* (3), 035002. <https://doi.org/10.1103/RevModPhys.89.035002>.
- (28) Casola, F.; van der Sar, T.; Yacoby, A. Probing Condensed Matter Physics with Magnetometry Based on Nitrogen-Vacancy Centres in Diamond. *Nat Rev Mater* **2018**, *3* (1), 1–13. <https://doi.org/10.1038/natrevmats.2017.88>.
- (29) Laraoui, A.; Ambal, K. Opportunities for Nitrogen-Vacancy-Assisted Magnetometry to Study Magnetism in 2D van Der Waals Magnets. *Appl. Phys. Lett.* **2022**, *121* (6), 060502. <https://doi.org/10.1063/5.0091931>.
- (30) Erickson, A.; Shah, S. Q. A.; Mahmood, A.; Fescenko, I.; Timalina, R.; Binek, C.; Laraoui, A. Nanoscale Imaging of Antiferromagnetic Domains in Epitaxial Films of Cr₂O₃ via Scanning Diamond Magnetic Probe Microscopy. *RSC Adv.* **2022**, *13* (1), 178–185. <https://doi.org/10.1039/D2RA06440E>.
- (31) Aslam, N.; Zhou, H.; Urbach, E. K.; Turner, M. J.; Walsworth, R. L.; Lukin, M. D.; Park, H. Quantum Sensors for Biomedical Applications. *Nat Rev Phys* **2023**, 1–13. <https://doi.org/10.1038/s42254-023-00558-3>.
- (32) Lovchinsky, I.; Sushkov, A. O.; Urbach, E.; de Leon, N. P.; Choi, S.; De Greve, K.; Evans, R.; Gertner, R.; Bersin, E.; Müller, C.; McGuinness, L.; Jelezko, F.; Walsworth, R. L.; Park, H.; Lukin, M. D. Nuclear Magnetic Resonance Detection and Spectroscopy of Single Proteins Using Quantum Logic. *Science* **2016**, *351* (6275), 836–841. <https://doi.org/10.1126/science.aad8022>.
- (33) Degen, C. L.; Poggio, M.; Mamin, H. J.; Rettner, C. T.; Rugar, D. Nanoscale Magnetic Resonance Imaging. *Proc. Natl. Acad. Sci. U.S.A.* **2009**, *106* (5), 1313–1317. <https://doi.org/10.1073/pnas.0812068106>.

- (34) Staudacher, T.; Shi, F.; Pezzagna, S.; Meijer, J.; Du, J.; Meriles, C. A.; Reinhard, F.; Wrachtrup, J. Nuclear Magnetic Resonance Spectroscopy on a (5-Nanometer)³ Sample Volume. *Science* **2013**, *339* (6119), 561–563. <https://doi.org/10.1126/science.1231675>.
- (35) Kehayias, P.; Jarmola, A.; Mosavian, N.; Fescenko, I.; Benito, F. M.; Laraoui, A.; Smits, J.; Bougas, L.; Budker, D.; Neumann, A.; Brueck, S. R. J.; Acosta, V. M. Solution Nuclear Magnetic Resonance Spectroscopy on a Nanostructured Diamond Chip. *Nat Commun* **2017**, *8* (1), 188. <https://doi.org/10.1038/s41467-017-00266-4>.
- (36) Smits, J.; Damron, J. T.; Kehayias, P.; McDowell, A. F.; Mosavian, N.; Fescenko, I.; Ristoff, N.; Laraoui, A.; Jarmola, A.; Acosta, V. M. Two-Dimensional Nuclear Magnetic Resonance Spectroscopy with a Microfluidic Diamond Quantum Sensor. *Sci. Adv.* **2019**, *5* (7), eaaw7895. <https://doi.org/10.1126/sciadv.aaw7895>.
- (37) Steinert, S.; Ziem, F.; Hall, L. T.; Zappe, A.; Schweikert, M.; Götz, N.; Aird, A.; Balasubramanian, G.; Hollenberg, L.; Wrachtrup, J. Magnetic Spin Imaging under Ambient Conditions with Sub-Cellular Resolution. *Nat Commun* **2013**, *4* (1), 1607. <https://doi.org/10.1038/ncomms2588>.
- (38) Simpson, D. A.; Ryan, R. G.; Hall, L. T.; Panchenko, E.; Drew, S. C.; Petrou, S.; Donnelly, P. S.; Mulvaney, P.; Hollenberg, L. C. L. Electron Paramagnetic Resonance Microscopy Using Spins in Diamond under Ambient Conditions. *Nat Commun* **2017**, *8* (1), 458. <https://doi.org/10.1038/s41467-017-00466-y>.
- (39) Nie, L.; Nusantara, A. C.; Damle, V. G.; Sharmin, R.; Evans, E. P. P.; Hemelaar, S. R.; Van Der Laan, K. J.; Li, R.; Perona Martinez, F. P.; Vedelaar, T.; Chipaux, M.; Schirhagl, R. Quantum Monitoring of Cellular Metabolic Activities in Single Mitochondria. *Sci. Adv.* **2021**, *7* (21), eabf0573. <https://doi.org/10.1126/sciadv.abf0573>.
- (40) Wojtas, D.; Li, R.; Jarzębska, A.; Sułkowski, B.; Zehetbauer, M.; Schafner, E.; Wierzbowski, K.; Mzyk, A.; Schirhagl, R. Quantum Sensing for Detection of Zinc-Triggered Free Radicals in Endothelial Cells. *Adv Quantum Tech* **2023**, *6* (11), 2300174. <https://doi.org/10.1002/qute.202300174>.
- (41) Nie, L.; Nusantara, A. C.; Damle, V. G.; Baranov, M. V.; Chipaux, M.; Reyes-San-Martin, C.; Hamoh, T.; Epperla, C. P.; Guricova, M.; Cigler, P.; Van Den Bogaart, G.; Schirhagl, R. Quantum Sensing of Free Radicals in Primary Human Dendritic Cells. *Nano Lett.* **2022**, *22* (4), 1818–1825. <https://doi.org/10.1021/acs.nanolett.1c03021>.
- (42) Wu, K.; Vedelaar, T. A.; Damle, V. G.; Morita, A.; Mougnaud, J.; Reyes San Martin, C.; Zhang, Y.; Van Der Pol, D. P. I.; Ende-Metselaar, H.; Rodenhuis-Zybert, I.; Schirhagl, R. Applying NV Center-Based Quantum Sensing to Study Intracellular Free Radical Response upon Viral Infections. *Redox Biology* **2022**, *52*, 102279. <https://doi.org/10.1016/j.redox.2022.102279>.
- (43) Mugnol, K. C. U.; Ando, R. A.; Nagayasu, R. Y.; Faljoni-Alario, A.; Brochsztain, S.; Santos, P. S.; Nascimento, O. R.; Nantes, I. L. Spectroscopic, Structural, and Functional Characterization of the Alternative Low-Spin State of Horse Heart Cytochrome *c*. *Biophysical Journal* **2008**, *94* (10), 4066–4077. <https://doi.org/10.1529/biophysj.107.116483>.
- (44) Mirkin, N.; Jaconic, J.; Stojanoff, V.; Moreno, A. High Resolution X-Ray Crystallographic Structure of Bovine Heart Cytochrome *c* and Its Application to the Design of an Electron Transfer Biosensor. *Proteins* **2007**, *70* (1), 83–92. <https://doi.org/10.1002/prot.21452>.
- (45) Hirota, S.; Hattori, Y.; Nagao, S.; Taketa, M.; Komori, H.; Kamikubo, H.; Wang, Z.; Takahashi, I.; Negi, S.; Sugiura, Y.; Kataoka, M.; Higuchi, Y. Cytochrome *c* Polymerization by Successive Domain Swapping at the C-Terminal Helix. *Proc. Natl. Acad. Sci. U.S.A.* **2010**, *107* (29), 12854–12859. <https://doi.org/10.1073/pnas.1001839107>.
- (46) Descostes, M.; Mercier, F.; Thromat, N.; Beaucaire, C.; Gautier-Soyer, M. Use of XPS in the Determination of Chemical Environment and Oxidation State of Iron and Sulfur Samples: Constitution of a Data Basis in Binding Energies for Fe and S Reference Compounds and Applications to the Evidence of Surface Species of an Oxidized Pyrite in a Carbonate Medium. *Applied Surface Science* **2000**, *165* (4), 288–302. [https://doi.org/10.1016/S0169-4332\(00\)00443-8](https://doi.org/10.1016/S0169-4332(00)00443-8).

- (47) Isaacson, Y. A.; Majuk, Z.; Brisk, M. A.; Gellender, M. E.; Baker, A. D. Iron to Sulfur Bonding in Cytochrome *c* Studied by X-Ray Photoelectron Spectroscopy. *J. Am. Chem. Soc.* **1975**, *97* (22), 6603–6604. <https://doi.org/10.1021/ja00855a067>.
- (48) Jarmola, A.; Acosta, V. M.; Jensen, K.; Chemerisov, S.; Budker, D. Temperature- and Magnetic-Field-Dependent Longitudinal Spin Relaxation in Nitrogen-Vacancy Ensembles in Diamond. *Phys. Rev. Lett.* **2012**, *108* (19), 197601. <https://doi.org/10.1103/PhysRevLett.108.197601>.
- (49) Mzyk, A.; Sigaeva, A.; Schirhagl, R. Relaxometry with Nitrogen Vacancy (NV) Centers in Diamond. *Acc. Chem. Res.* **2022**, *55* (24), 3572–3580. <https://doi.org/10.1021/acs.accounts.2c00520>.
- (50) Ziem, F. C.; Götz, N. S.; Zappe, A.; Steinert, S.; Wrachtrup, J. Highly Sensitive Detection of Physiological Spins in a Microfluidic Device. *Nano Lett.* **2013**, *13* (9), 4093–4098. <https://doi.org/10.1021/nl401522a>.
- (51) Kleinsasser, E. E.; Stanfield, M. M.; Banks, J. K. Q.; Zhu, Z.; Li, W.-D.; Acosta, V. M.; Watanabe, H.; Itoh, K. M.; Fu, K.-M. C. High Density Nitrogen-Vacancy Sensing Surface Created via He⁺ Ion Implantation of ¹²C Diamond. *Appl. Phys. Lett.* **2016**, *108* (20), 202401. <https://doi.org/10.1063/1.4949357>.
- (52) Huang, L.-C. L.; Chang, H.-C. Adsorption and Immobilization of Cytochrome *c* on Nanodiamonds. *Langmuir* **2004**, *20* (14), 5879–5884. <https://doi.org/10.1021/la0495736>.
- (53) Mrózek, M.; Rudnicki, D.; Kehayias, P.; Jarmola, A.; Budker, D.; Gawlik, W. Longitudinal Spin Relaxation in Nitrogen-Vacancy Ensembles in Diamond. *EPJ Quantum Technol.* **2015**, *2* (1), 1–11. <https://doi.org/10.1140/epjqt/s40507-015-0035-z>.
- (54) Laraoui, A.; Hodges, J. S.; Meriles, C. A. Nitrogen-Vacancy-Assisted Magnetometry of Paramagnetic Centers in an Individual Diamond Nanocrystal. *Nano Lett.* **2012**, *12* (7), 3477–3482. <https://doi.org/10.1021/nl300964g>.
- (55) Laraoui, A.; Meriles, C. A. Approach to Dark Spin Cooling in a Diamond Nanocrystal. *ACS Nano* **2013**, *7* (4), 3403–3410. <https://doi.org/10.1021/nn400239n>.
- (56) Sangtawesin, S.; Dwyer, B. L.; Srinivasan, S.; Allred, J. J.; Rodgers, L. V. H.; De Greve, K.; Stacey, A.; Dontschuk, N.; O'Donnell, K. M.; Hu, D.; Evans, D. A.; Jaye, C.; Fischer, D. A.; Markham, M. L.; Twitchen, D. J.; Park, H.; Lukin, M. D.; de Leon, N. P. Origins of Diamond Surface Noise Probed by Correlating Single-Spin Measurements with Surface Spectroscopy. *Phys. Rev. X* **2019**, *9* (3), 031052. <https://doi.org/10.1103/PhysRevX.9.031052>.
- (57) Ariyaratne, A.; Bluvstein, D.; Myers, B. A.; Jayich, A. C. B. Nanoscale Electrical Conductivity Imaging Using a Nitrogen-Vacancy Center in Diamond. *Nat Commun* **2018**, *9* (1), 2406. <https://doi.org/10.1038/s41467-018-04798-1>.
- (58) Hall, L. T.; Kehayias, P.; Simpson, D. A.; Jarmola, A.; Stacey, A.; Budker, D.; Hollenberg, L. C. L. Detection of Nanoscale Electron Spin Resonance Spectra Demonstrated Using Nitrogen-Vacancy Centre Probes in Diamond. *Nat Commun* **2016**, *7* (1), 10211. <https://doi.org/10.1038/ncomms10211>.
- (59) Shi, F.; Zhang, Q.; Wang, P.; Sun, H.; Wang, J.; Rong, X.; Chen, M.; Ju, C.; Reinhard, F.; Chen, H.; Wrachtrup, J.; Wang, J.; Du, J. Single-Protein Spin Resonance Spectroscopy under Ambient Conditions. *Science* **2015**, *347* (6226), 1135–1138. <https://doi.org/10.1126/science.aaa2253>.
- (60) Pessoa, J. Live-Cell Visualization of Cytochrome *c* : A Tool to Explore Apoptosis. *Biochemical Society Transactions* **2021**, *49* (6), 2903–2915. <https://doi.org/10.1042/BST20211028>.
- (61) Trusheim, M. E.; Li, L.; Laraoui, A.; Chen, E. H.; Bakhru, H.; Schröder, T.; Gaathon, O.; Meriles, C. A.; Englund, D. Scalable Fabrication of High Purity Diamond Nanocrystals with Long-Spin-Coherence Nitrogen Vacancy Centers. *Nano Lett.* **2014**, *14* (1), 32–36. <https://doi.org/10.1021/nl402799u>.
- (62) B J Lindberg; K Hamrin; G Johansson; U Gelius; A Fahlman; C Nordling; K Siegbahn. Molecular Spectroscopy by Means of ESCA II. Sulfur Compounds. Correlation of Electron Binding Energy with Structure. *Phys. Scr.* **1970**, *1* (5–6), 286–298. <https://doi.org/10.1088/0031-8949/1/5-6/020>.
- (63) Karki, P. B.; Timalina, R.; Dowran, M.; Aregbesola, A. E.; Laraoui, A.; Ambal, K. An Efficient Method to Create High-Density Nitrogen-Vacancy Centers in CVD Diamond for Sensing Applications. *Diamond and Related Materials* **2023**, 110472. <https://doi.org/10.1016/j.diamond.2023.110472>.